

Linearly dispersive bands at the onset of correlations in K_xC_{60} films

Ping Ai,¹ Luca Moreschini,^{1,2} Ryo Mori,¹ Drew W. Latzke,^{1,2} Jonathan D. Denlinger,³ Alex Zettl,^{1,2,4} Claudia Ojeda-Aristizabal,⁵ and Alessandra Lanzara^{1,2,*}

¹*Materials Sciences Division, Lawrence Berkeley National Laboratory, Berkeley, California 94720, United States*

²*Department of Physics, University of California, Berkeley, California 94720, United States*

³*Advanced Light Source, Lawrence Berkeley National Laboratory, Berkeley, California 94720, United States*

⁴*Kavli Energy NanoSciences Institute at the University of California, Berkeley,*

and the Lawrence Berkeley National Laboratory, Berkeley, California 94720, United States

⁵*Department of Physics and Astronomy, California State University, Long Beach, California 90840, United States*

(Dated: May 30, 2023)

Molecular crystals are a flexible platform to induce novel electronic phases. Due to the weak forces between molecules, intermolecular distances can be varied over relatively larger ranges than interatomic distances in atomic crystals. On the other hand, the hopping terms are generally small, which results in narrow bands, strong correlations and heavy electrons. Here, by growing K_xC_{60} fullerides on hexagonal layered Bi_2Se_3 , we show that upon doping the series undergoes a Mott transition from a molecular insulator to a correlated metal, and an in-gap state evolves into highly dispersive Dirac-like fermions at half filling, where superconductivity occurs. This picture challenges the commonly accepted description of the low energy quasiparticles as appearing from a gradual electron doping of the conduction states, and suggests an intriguing parallel with the more famous family of the cuprate superconductors. More in general, it indicates that molecular crystals offer a viable route to engineer electron-electron interactions.

Molecular assemblies are appealing systems for engineering correlations since, intermolecular forces being typically weak, they can often be patterned in a desired way by an appropriate choice of the substrate. As a notable example, C_{60} can be grown on a number of substrates, resulting in different lattice mismatch, moiré periodicities, rotational order and contact geometries between the C_{60} molecules [1–5]. Such flexibility allows acting on the balance between the on-site Coulomb repulsion U and the bandwidth W , thereby tuning correlations and driving qualitatively different ground states. In this sense, self-assembling molecular crystals can represent a valid alternative to the recently discovered twisted-layer structures of graphene or transition metal dichalcogenides, [6–10]. Although these have the quality of lending themselves naturally to gating experiments, the ability to select a given ground state relies on the precise control of the twist angle, which is difficult and also incompatible with any bottom-up fabrication technique, since that would necessarily privilege the rotational alignment of the layers.

Here we focus on the family of the A_xC_{60} fullerides, where fullerene molecules act as anions and other elements, often alkali metals, act as cations. The majority of the A_xC_{60} compounds are known to transition from insulating to metallic for increasing x as the $C t_{1u}$ molecular orbitals get progressively filled [13–15]. The trivalent members are mostly metallic and superconducting, but can be antiferromagnetic insulators for large intermolecular distances. The proximity of superconductivity to a Mott insulating ground state suggested the possibility that its nature, which remains to this day uncertain, may not be that of conventional BCS theory and derive

instead from electron-electron interactions, bearing similarities with the case of other unconventional superconductors [14–20].

Although the effect of electron doping by alkali metals has already been studied in many instances by photoemission, providing evidence of a clear departure from a rigid band shift [21–23], the lack of angular resolution has left many fundamental unanswered questions on how the metallic state emerges, what the nature of the low energy excitations is, and how correlated states such as superconductivity develop from this metallic phase. Part of the difficulty associated with revealing the mechanisms behind these open questions is that, similarly to what happens in other C-based structures, such as graphene [6, 24, 25], the low energy states of K_3C_{60} appear to be extremely dependent on small modifications of the crystal structure, substrate or preparation conditions. In addition, the growth of A_xC_{60} samples is known to be prone to phase separation [26, 27]. Indeed, the sparse photoemission measurements available present a remarkable variety of results both for angle-integrated [28] and angle-resolved photoemission (ARPES) studies, spanning from a clear hole-like dispersion reported in films grown on $Ag(111)$ [29], electron-like states on $Ag(100)$ [30] to a very shallow electron pocket on $Cu(111)$ [31].

Here, by using ARPES on *in situ* grown films, we found that when doped C_{60} molecules are deposited on top of the layered topological insulator Bi_2Se_3 , a molecular subband develops, equivalent to a lower Hubbard band in a Mott scenario, accompanied by the evolution from massive to nearly massless quasiparticles as half filling is approached. These results place K_3C_{60} in the regime of correlated metals, and point to the A_xC_{60} series as a plat-

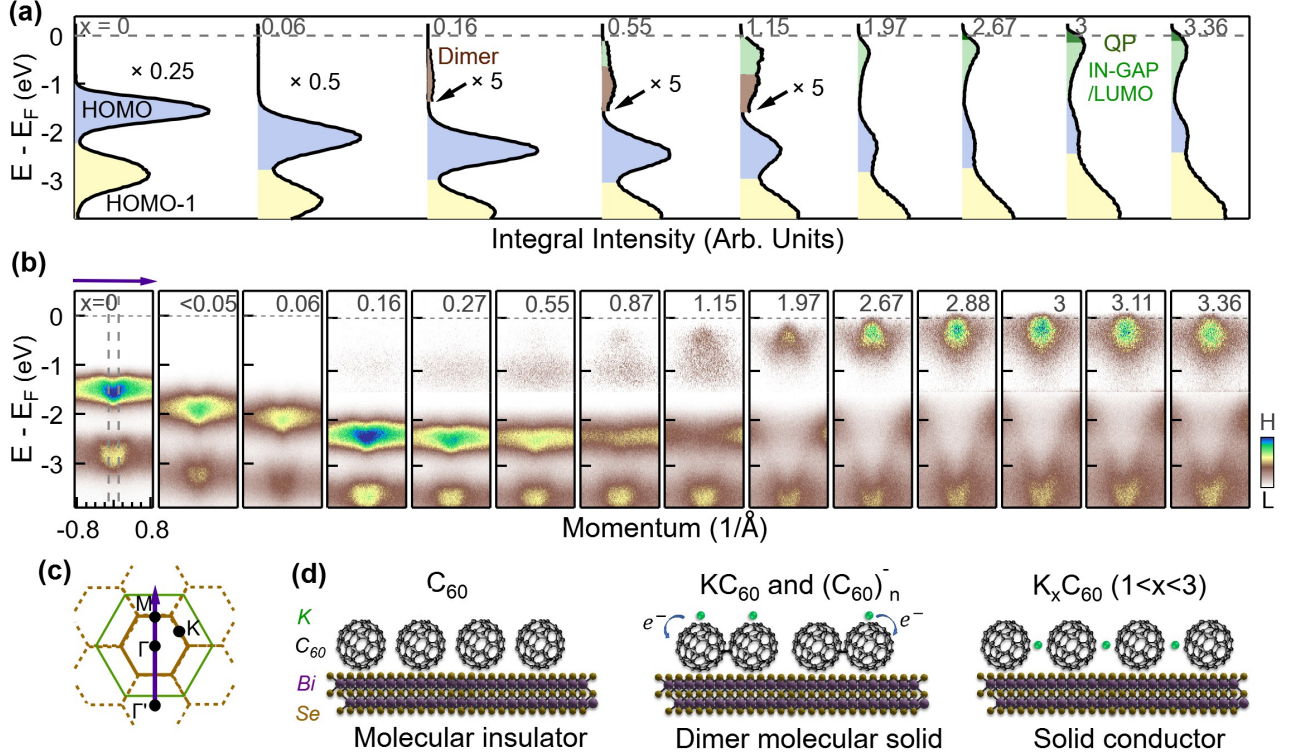


FIG. 1. (a) Photoemission intensity integrated over a narrow range at Γ , indicated by dashed lines in the left panel of (b). The doping value is indicated at the top of each panel and is estimated from the intensity of the K 3p levels, as explained in Ref. [11]. Some curves are rescaled by the numbers indicated. The different colors indicate the approximate energy range of the electronic states described in the text. (b) ARPES dispersion along the ΓM direction, as marked in the BZ in (c). For $x > 0.06$ the intensity above and below $E = -1.4$ eV is separately rescaled by a factor of 10 and 2, respectively, to enhance the signal for the low energy states. (c) The 1st (solid lines) and the 2nd BZ (dashed lines) of the sample. The green lines indicate the first BZ of Bi_2Se_3 for reference. (d) Pictorial illustration of the transition from a molecular insulator to a solid conductor with the intermediate formation of dimerized pairs. For the distance between the C_{60} molecules in the plane we assume 9.66 \AA [12], which yields $\Gamma M \simeq 0.32 \text{ \AA}^{-1}$.

form where highly dispersive, Dirac-like electrons coexist with, and possibly can be tuned or driven by, electron-electron interactions.

The samples measured in this work are K_xC_{60} films with a thickness of five monolayers grown on $Bi_2Se_3(0001)$, as described in the methods section [11] and in Ref. [32]. The C_{60} molecules arrange along the (111) orientation in the same *fcc* structure as in the bulk, but with a $\sim 3.4\%$ compressed lattice. Upon doping, the alkali ions progressively fill in the spaces in between the buckyballs until, for $x = 3$, they form three hexagonal lattice layers for each C_{60} layer, with *abab* stacking [33]. The dispersion of the electronic bands remains mostly confined within the (111) planes (Supplementary Fig.S3)) and therefore we will discuss the data referring to the hexagonal surface Brillouin zone (BZ) of Fig. 1(c).

The evolution of the electronic structure of K_xC_{60} from the insulating C_{60} to slightly above the “optimal” metallic state at half filling ($x = 3$) is shown as a series of

angle-integrated photoemission spectra in Fig. 1(a) and as ARPES maps along the ΓM direction, measured with *p* polarization, in Fig. 1(b). In the angle-integrated data, the two peaks at $x = 0$ are associated with the highest occupied molecular orbital (HOMO) and the next highest occupied molecular orbital (HOMO-1). Adding potassium, which ionizes and donates one charge per atom to the molecular solid [34], for low doping levels both the HOMO and HOMO-1 spectral features shift toward higher binding energy as expected for a standard rigid band shift description upon electron doping, as well established from previous work [21–23]. The binding energy of the states is irrelevant in this regime since it depends on the pinning of the Fermi level (E_F) in the ~ 1.6 eV band gap, further widened by the poor screening of the photohole [23].

For $x > 0.16$, a new in-gap state develops ~ 1 eV below the Fermi level (brown in Fig. 1(a)). Its existence only over a finite doping range, $0.16 < x < 1.2$, and its

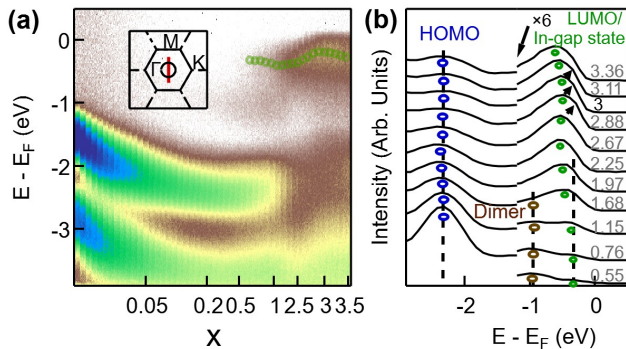


FIG. 2. (a) Detailed doping dependence of the ARPES spectra measured along ΓM , as indicated in the inset, with p -polarized light. (b) A subset of the spectra zoomed in to the in-gap-state, dimer and HOMO states. The arrows for the spectra in proximity of $x = 3$ point to the shoulder of the LUMO/in-gap state peak due to the metallic quasiparticle.

separation of ~ 1.2 eV from the HOMO band (measured as peak-to-peak distance) suggests that it be related to the partial formation of C_{60} dimer pairs that can be stabilized below 270K and prevents a simple metallic state in K_1C_{60} [35–39]. For $x > 0.5$, an additional in-gap state emerges at ~ -0.5 eV (green in Fig. 1(a)), and in parallel an overall redistribution of the spectral intensity occurs between the HOMO and HOMO-1 bands. As we will show later (Fig. 1(b) and Fig. 3), this hybridization of the two molecular HOMO and HOMO-1 localized bands into a highly dispersive band for $x > 1.5$, much more dramatic than predicted by theory [40], marks the departure from a narrow bandwidth molecular orbital picture and the formation of a solid crystal as schematically illustrated in (Fig. 1(d)). As the doping approaches $x = 3$, a point which coincides with the minimum resistivity and superconductivity [22, 28], the in-gap state spectral weight is maximum and it crosses the Fermi level.

While the presence of both the insulating and metallic states has been previously reported, their origin has been matter of debate for a long time [13, 41, 42]. Approaching the problem from band theory, the insulating phase for $x=2,4$ cannot be explained since the series is all expected to be metallic due to the partial filling of the t_{1u} manifold. Conversely, starting from a Mott-Hubbard approach it is the metallic phase for $x=3$ that is equally puzzling, since the Coulomb repulsion U is more than twice the t_{1u} bandwidth W (~ 0.5 eV) [43]. To unambiguously understand how metallicity develops, it is critical to have access to the energy and momentum dependence of each state upon doping of the t_{1u} manifold. We show in Fig. 1(b) such a study for the first time.

The data reveal a clear difference between the two in-gap states. Specifically, while the first one at ~ -1 eV is strongly localized, the second state in proximity of the

Fermi level is clearly dispersive, and its band velocity appears to increase approaching half filling, while its binding energy decreases (as discussed in detail later, see Supplementary Fig. S6). This doping dependence supports an intriguing scenario where the near- E_F states are associated with the formation of a lower Hubbard band driven by correlations and are responsible for the transition to the insulating phase of a solid crystal on both sides of half filling (K_2C_{60} and K_4C_{60}). This sets the K_xC_{60} fulleride series within a Mott transition framework on both sides of $x = 3$, clearly different from the commonly accepted description where the low energy states are assigned to a lowest unoccupied molecular orbital (LUMO)-derived band, centered above E_F , which shifts into the occupied states as the doping increases, and the transition is interpreted in a band filling picture [22, 23].

The doping dependence of the near- E_F spectra is shown in Fig. 2 as an image plot of the ARPES intensity integrated over the momentum range along ΓM indicated by the red line in the inset. All the spectral features mentioned in Fig. 1 very rapidly shift to higher binding energy (note the non linear scale for the x axis) and starting from $x \simeq 1$ they start to gradually drift back toward E_F . The shift to higher binding energies pins the Fermi level to the bottom of the unoccupied LUMO states [22, 23], whereas the opposite shift (Fig. 2(b)), not as clear in previous work and instead evident here, is almost certainly due to the more efficient screening approaching the metallic phase compared to that in the insulating one(s).

At half filling, the quasiparticle weight also includes contributions from LUMO-derived states. In this regime the distinction between Hubbard bands and in-gap state is of course ill-defined as the states hybridize and close the gap [44]. The fact that this doping level also corresponds to the appearance of superconductivity represents an intriguing analogy with the case of cuprates, where the Fermi surface is best defined in the normal state at optimal doping, at the maximum of the superconducting dome.

In Fig. 3(a,b) we compare the ARPES spectra along the ΓM direction at the two extremes of the undoped insulating phase of C_{60} and of the optimally doped metallic phase of K_3C_{60} . As discussed in Fig. 1(b), in the optimally doped phase, the merging of the C_{60} molecular electronic levels with a bandwidth of < 0.5 eV, into a single dispersive band with an overall bandwidth of ~ 2 eV for K_3C_{60} is observed. The K atoms therefore increase substantially the hopping terms between different fullerene buckyballs and the resulting bandwidth is now determined by the energy scale of the intermolecular forces [13]. Indeed, because of the hybridization between the two manifolds, the description of the orbital composition following the I_h icosahedral symmetry and the strict separation between π_5 (H-type) character for the HOMO states and π_4 (G-type) for the HOMO-1 states (Ref. [12])

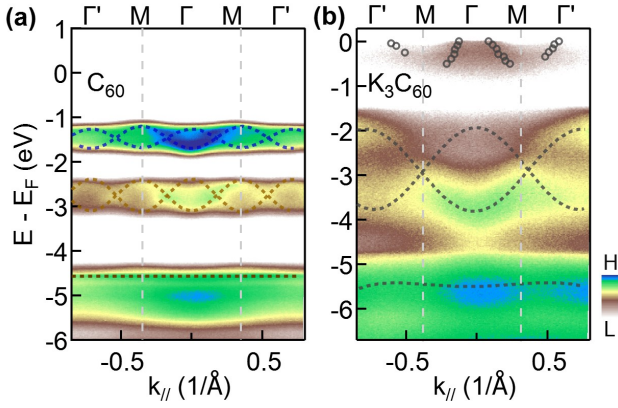


FIG. 3. (a) Band dispersion of undoped C_{60} measured with p -polarized light. The dashed curves are guides to the eye following the dispersion of the HOMO states (for details see Ref. [32]). (b) Same as (a) for K_3C_{60} . The symbols in the Fermi level region indicate the peak positions from MDC fits. Note that the energy scale in (b) is shifted by 0.7 eV relatively to that in (a) to align the HOMO/HOMO1 states.

is no longer valid. Such hybridization is well visible also in the circular dichroism (CD) signal (See supplementary Fig. S7).

At half filling an additional state can be extracted from the momentum distribution curve (MDC) fits, overlapped to the image (see markers in Fig. 3(b)), which shows hole-like dispersion. At first sight it is reminiscent of the dispersive bands already reported for K_3C_{60} grown on Ag(111) [29, 30], yet a side by side comparison (Supplementary Fig. S4) reveals that the two cases are distinct with a difference in Fermi velocity of over 70% and a band minimum shallower than 0.2 eV in Ref. [29] *vs.* a bandwidth larger than 0.4 eV in the present study.

In Fig. 4(a,b), we report a high statistics image measured along ΓM across two BZs for $x = 3$. In contrast to the parabolic dispersion at lower doping, the data reveal a linear dispersion over the whole energy range up to 0.5 eV (see also supplementary Fig. S4), and is reminiscent of massless Dirac fermions. The exact dispersion is extracted in a quantitative way by using a standard Lorentzian fitting of the momentum distribution curves in Fig. 4(c,d). From a linear fit of the peak positions we find a Fermi velocity $v_F = (7.1 \pm 0.6) \times 10^5 \text{ ms}^{-1}$, comparable to some of the highest values reported for Dirac materials [25, 45–51] (see Fig. 4(e)). The position of the crossing point can be determined by extrapolating the dispersion to the unoccupied states, and is estimated to be $(0.3 \pm 0.1) \text{ eV}$ above the Fermi level. The constant energy maps (k_x *vs.* k_y), shown in Fig. 4(f), as well as the radial MDC fits of Fig. 4(g), prove the isotropic nature of the dispersion in the surface plane. Finally, the integrated spectral weight, which is proportional to the

occupied density of states, as plotted in Fig. 4(h), reveals the same linear dependence as a function of the binding energy characteristic of Dirac fermions [53], in contrast to the more parabolic dispersion at lower doping. This description holds for a narrow doping range, with a transition to a parabolic hole-like dispersion for $1 < x < 2.7$ (Fig. 1(b)).

Since fullerides are widely studied materials and can be grown on a number of substrates, we are left with educated guesses of the reasons why the linearly dispersive states at Γ have not been reported before. The Bi_2Se_3 substrate used here is known to reduce the rotational disorder of the C_{60} molecules [32], and induces a compressive strain which lowers the intermolecular distance by $\sim 3.4\%$ with respect to the bulk value. This unusual situation (most substrates induce a tensile strain, see Supplementary Table S1) results in an increase of the bandwidth W , which is known to increase with the inverse of the intermolecular distance. Whereas on Ag(111) and Ag(100) values of $\sim 0.25 \text{ eV}$ were found [29, 30, 54], here we extract a lower limit for W of 0.4 eV from the occupied portion of the t_{1u} states, and up to $0.5 - 0.7 \text{ eV}$ depending on the (non accessible) dispersion above the Fermi level. The Coulomb repulsion U on the other hand is less straightforward to estimate from ARPES and would require a more involved analysis and comparison with Auger spectroscopy [55]. A dedicated theoretical treatment would be welcome to determine if the increase of W is accompanied here by a lowering of the U/W ratio, which may be the culprit of the observed emergence of carriers of higher mobility at Γ . On the experimental side, a meaningful term of comparison will be provided by the recently synthesized fullerene crystals where the C_{60} molecules are covalently bonded and the intermolecular distance is reduced with respect to that in the *fcc* lattice [56, 57].

Regardless of the microscopic origin of the Dirac-like dispersion, the results presented reveal a transition from slow and massive electrons to fast and nearly massless quasiparticles which coexist and possibly are driven by electronic correlations. These findings put forward the exciting proposal that molecular crystals, with their adaptability to be patterned on multiple substrates, and in particular A_3C_{60} compounds where even slight modifications of the bandwidth are known to result in different ground states, can provide a new flexible way to engineer correlations. In addition, the emergence of a metallic phase from an in-gap state in a fashion typical of a Mott transition hints at fascinating analogies with the case of superconducting cuprates. Interesting future developments will be to figure out how robust such massless fermions are in dependence of the intermolecular distance, as well as to explore the physics in the thin film limit, where the moiré potential would become important. K_3C_{60} appears to be close to a sweet spot where the interplay between U and W allows for a crossover

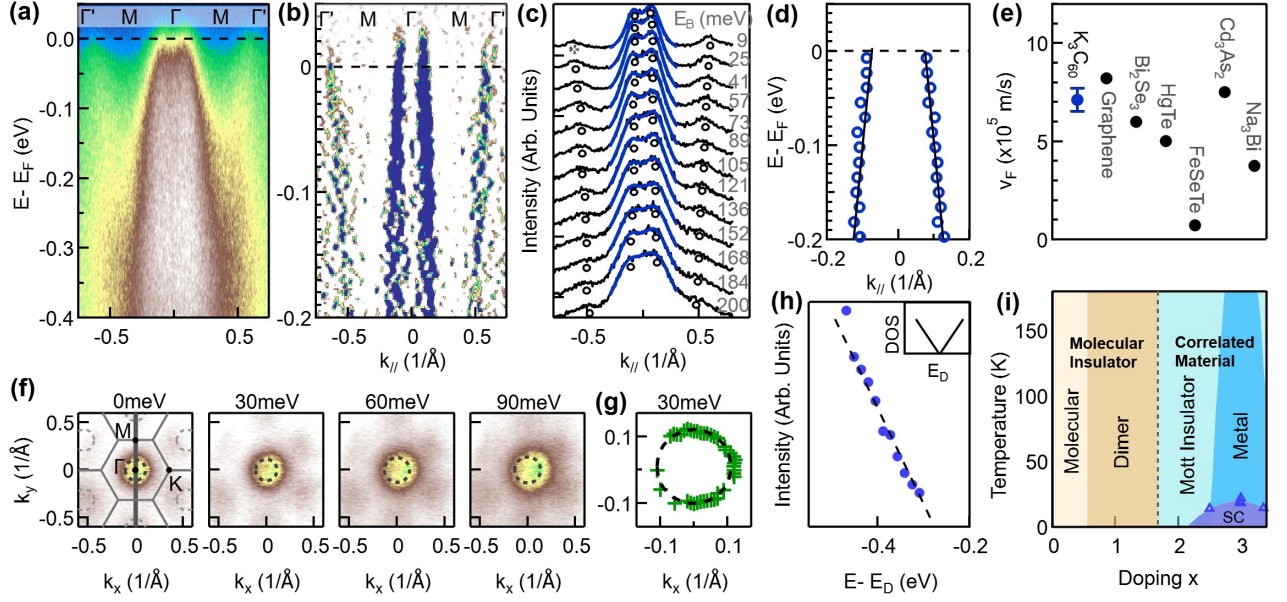


FIG. 4. (a,b) Low energy states of K_3C_{60} along ΓM shown as an ARPES intensity map and a second derivative plot. (c) MDC stack in the same energy region, with the binding energy in meV indicated for each spectrum. The black curves are the ARPES data while the blue curves are best fits in a narrow energy interval around Γ by a double Lorentzian function. The circles indicate the approximate peak positions. (d) The same circles reproduced together with a fit with a power function $E_D + A \cdot |x|^b$, where E_D is the energy of the crossing point and the exponent b is not constrained. The best fit was found for $b \simeq 1.1$, very close to a linear function. The Fermi velocity from the closest linear fit is plotted in (e) together with that of several Dirac materials, and namely graphene [25, 45], Bi_2Se_3 [46], $HgTe$ [47], $FeSe_{0.45}Te_{0.55}$ [48], Cd_3As_2 [49, 50] and Na_3Bi [51]. (f) Constant energy contours at different binding energies up to 270 meV. The dashed circles in the left panel mimic the contours in the 2nd BZs. (g) Peak positions from radial fits of the constant energy contour at 30 meV. (h) density of states as a function of the energy separation from the estimated crossing point, extracted from the integrated ARPES intensity. (i) Tentative phase diagram of K_xC_{60} as a function of doping x . The blue triangles are from Ref. [52], we did not investigate the presence of superconductivity in our films.

between an insulator and a correlated metal.

ACKNOWLEDGMENTS

This work was primarily funded by the U.S. Department of Energy (DOE), Office of Science, Office of Basic Energy Sciences, Materials Sciences and Engineering Division under contract No. DE-AC02-05-CH11231 (Ultrafast Materials Science program KC2203). A.L. was partially supported as part of the Center for Novel Pathways to Quantum Coherence in Materials, an Energy Frontier Research Center funded by the US Department of Energy, Office of Science, Basic Energy Sciences. A.L. and L.M. also acknowledge support for sample growth from the Gordon and Betty Moore Foundation's EPIQS Initiative through Grant No. GBMF4859. C.O.-A. was funded for data acquisition by DOE Office of Science, Office of Basic Energy Sciences under Contract No. DE-SC0018154. Sample growth was supported by the U.S. Department of Energy, Office of Sci-

ence, Office of Basic Energy Sciences, Materials Sciences and Engineering Division under contract No. DE-AC02-05-CH11231, within the Van der Waals Heterostructures Program (KCWF16). The Advanced Light Source is supported by the DOE Office of Science User Facility under contract No. DEAC02-05CH11231.

SUPPLEMENTARY MATERIALS

Materials and methods

High-quality C_{60} thin film samples were grown *in situ* in ultrahigh vacuum on a bulk Bi_2Se_3 substrate as detailed elsewhere [32]. The film thickness was ~ 50 Å. Potassium deposition is done *in situ* with a getter alkali evaporator. The angle-resolved and angle-integrated spectra are collected after each single deposition controlled by a timed shutter. The doping level is not linear with the dosing sequence and is estimated based on the relative ratio of the K 3p core level intensity with

respect to the optimum doping ($x = 3$) spectra. The latter is identified by the maximum value of the ratio between LUMO and HOMO band, in line with previous reports [22]). Note that, in view of our findings here, the LUMO intensity should be better identified as an in-gap (G) state, which hybridizes with the LUMO states only in proximity of half filling. High resolution ARPES experiments were performed at Beamline 4.0.3 (MERLIN) of the Advanced Light Source using 45 eV linearly or circularly polarized photons, and 70 eV photons (in supplementary Fig. S7) in vacuum better than 5×10^{-11} Torr. The total-energy resolution was 20 meV with an angular resolution ($\Delta\theta$) of $\leq 0.2^\circ$. Data were taken at 200 K during K-dosing and then cooled to 30 K for the high statistics maps of the massless states. No obvious change was noticed lowering the temperature except for a trivial sharpening of the spectral features.

Energy shifts upon electron doping

In Fig. S1 we show the evolution of the angle integrated photoemission spectra from undoped C_{60} to a doping level of $x = 3.36$. Overall, until the appearance of the G+LUMO states all the peaks including the K $3p$ level follow a rigid shift, as observed in previous photoemission studies [22, 23, 28]. A more detailed dependence of the G+LUMO and HOMO energy shifts for doping levels approaching $x = 3$ is shown in Fig. 2 of the main text.

Note that the energy shift changes sign as the sample starts to become more metallic, due to increased screening of the core hole, and that the HOMO and HOMO-1 peaks tend to merge, and same for the HOMO-4 and HOMO-5 features, as the addition of the K atoms increases the overlap between wavefunctions of different C_{60} molecules and causes a departure from the molecular orbital description of the electronic levels.

Doping level calibration

Although it is known to vary as a function of the photon energy, the ratio between the photoemission intensity of the G+LUMO and HOMO states in the K_xC_{60} series is highest for $x = 3$ [22]. In Fig. S2 we show separately the intensity of G+LUMO, HOMO and K $3p$ levels extracted from the angle integrated photoemission data, as well as the (G+LUMO)/HOMO ratio. The doping level is then calibrated relative to the maximum ratio. While this estimate has some margin of error, this is certainly lower than for a calibration based on the deposition time, since the alkali atoms may not distribute uniformly across the layers. Note also that the first deposition cycles result into a large shift of the electronic levels (see Fig. S1) even though the K $3p$ is not yet visible in the spectra.

Photoemission intensity oscillation of C_{60} and K_3C_{60}

The photon-energy dependences of photoemission intensities of C_{60} were observed and discussed in previous papers [12, 60–63]. Because of the unique molecular structure like a spherical shell and the large size of C_{60} , the photoemission intensity shows an oscillation for each molecular orbitals, as shown in Fig. S3. Density functional theory (DFT) and time dependent DFT level (TDDFT) calculations considering the $\sigma - \pi$ symmetries of the ionized orbitals were carried out, which demonstrated the single-particle origin of the oscillations [63].

Here we compare the dependence on the surface-normal momentum of the photoemission intensity for C_{60} and K_3C_{60} as total intensity (Fig. S3(a)) and as ratios of (G+LUMO)/HOMO, HOMO/HOMO-1 and HOMO-2/HOMO-1 (Fig. S3(b,c)) to help reduce the influence of the cross section variation. Clearly, although there are some differences among the overall intensity trends, the period of the k_z oscillations is still dominated by the molecular properties of the C_{60} molecule rather than by the period of the fcc crystal structure, which would result instead in a $\sim 0.78 \text{ \AA}^{-1}$ periodicity

Linear dispersion at Γ

Figure S4 shows the raw ARPES data on a larger energy scale than in the 2nd derivative data of Fig. 3(a). The linear dispersion is better visible in the close-up in (b, c), where one branch at the side Γ' points is also present at $|k_{||}| \simeq 0.7 \text{ \AA}^{-1}$. The bands are hole-like but have a qualitatively different dispersion than that reported in Ref. [29] for K_3C_{60} on a Ag(111) substrate, as evident in the comparison of (c). The latter data were taken on a single ML, even though the role of thickness in shaping the dispersion was not addressed. Extracting the Fermi velocity for the two cases we find $1.6 \times 10^5 \text{ ms}^{-1}$ for K_3C_{60} in Ref. [29] *vs.* $7.1 \times 10^5 \text{ ms}^{-1}$ in the present study.

Ruling out the presence of Dirac states from the substrate

Figure S5 shows the Dirac cone of Bi_2Se_3 as its intensity fades upon increasing thickness of the C_{60} film. Note that the crossing is in the occupied states at a very different energy than the one extracted for K_3C_{60} , and that the Dirac cone is completely suppressed for a thickness of 3 MLs, lower than the 5 MLs of the films studied here. Therefore the possibility that the low energy states would originate from the substrate can be ruled out.

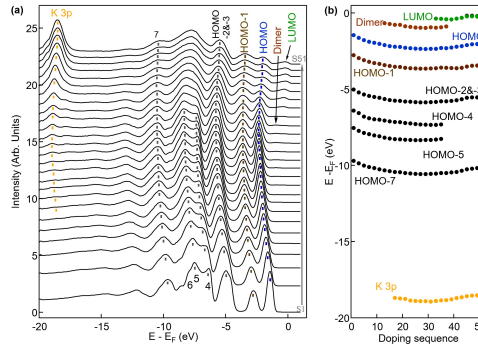


FIG. S1. **a** Angle-integrated photoemission spectra shown for increasing K doping. See the main paper for the assignment of the peaks at low binding energy. The peaks labeled with 4-7 are assigned as common practice for the C_{60} molecular levels[58, 59]. **b** Doping dependence of the peak binding energy of each occupied state from a fit of the spectra in **a**.

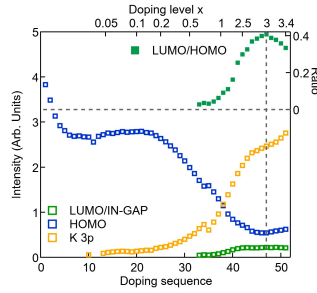


FIG. S2. **Doping level calibration.** The solid green squares represent the $(G+LUMO)/HOMO$ intensity ratio. The point correspondent to the largest ratio is labeled $x = 3[22]$. Separate intensities for $G+LUMO$ (green), $HOMO$ (blue) and $K\ 3p$ (yellow) band are shown below.

Crystal structure and in-gap band velocity

Comparing the lattice constants of C_{60} and Bi_2Se_3 we find that 3 times the C_{60} intermolecular distance is equivalent to ~ 7 times the in-plane Se-Se distance for Bi_2Se_3 (Fig. S6(a)). This is consistent with the LEED pattern shown in Fig. S6(b) and with the ratio of the distances between the center and the reciprocal lattice points. Such reconstruction would mean for the C_{60} films a 3.4% compression compared to the bulk fcc value. This value is well within the range of the compressions/expansions observed on other substrates (see Table S1) and therefore we consider this a reasonable assumption for an epitaxially grown film.

As mentioned in main manuscript, the band velocity increases with increasing doping. Here we plot second derivative data taken along the momentum direction in the doping range $x \simeq 1.15 - 2.88$, and extract the band velocity as $E = v \cdot k_{\parallel}$. We do so assuming a linear dispersion for consistency across the doping range in Fig. S6(c) to simplify the comparison, even though the dispersion appearing linear at low doping levels is an artifact of the derivative along the momentum axis. Note that,

as reported in numerous instances, the second derivative data are more reliable for highly dispersive features when the derivative is applied along the momentum direction, and viceversa for bands with small dispersion when the derivative is applied along the energy axis. The results plotted in Fig. S6(d), along with an upward energy shift for increasing doping, clearly show an increase of the band velocity, and in particular a rather sudden jump, with a $>35\%$ change, at $x \sim 3$, where correlations and superconductivity develop.

Circular dichroism of HOMO/HOMO-1 states

As mentioned in the main text, the change in orbital character is also consistent with the circular dichroism (CD) signal from the HOMO/HOMO-1 states. In K_3C_{60} (Fig. S7(b)) a single CD texture spans the whole bandwidth, supporting that the dispersion is associated with a single band, as opposed to undoped C_{60} (Fig. S7(a)), where the HOMO and HOMO-1 bands exhibit a clearly distinct CD signal [12]. Note that the transition to de-

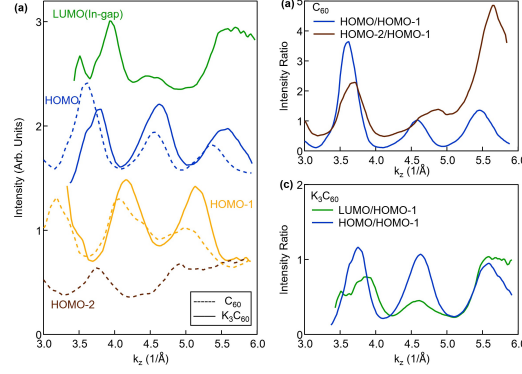


FIG. S3. **Photoemission intensity oscillation of C_{60} and K_3C_{60} .** **a** The intensity oscillation G plus LUMO (green), HOMO (blue), HOMO-1 (yellow), and HOMO-2 (brown) from C_{60} (dashed lines) and K_3C_{60} (solid lines). **b** shows the intensity ratio of HOMO/HOMO-1 and HOMO-2/HOMO-1 for normalization before doping. **c** shows the same for doped K_3C_{60} , but for (G+LUMO)/HOMO-1 and HOMO/HOMO-1.

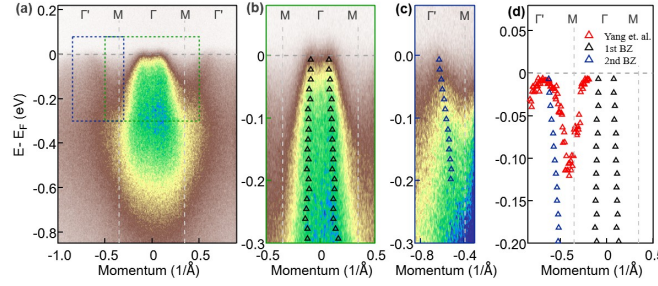


FIG. S4. **a** ARPES map along the ΓM high-symmetry direction, same as in Fig. 3 of the main text with larger energy and momentum range. **b** Close-up to the range indicated by the green dashed box in (a) (the 1st BZ) with fitted dispersion, same as in Fig. 3(a) of the main text. **c** As same as (b), but for the 2nd BZ (blue dashed box), with a different color contrast. **d** Fitted band dispersion from this work compared to the band dispersion from the previous Ref. [29], shown as red triangles.

localized states can be also indirectly inferred from the ARPES matrix elements of Fig. 3(b): in K_3C_{60} they nearly suppress the band maximum in the first BZ, yielding an apparent periodicity twice as large as the one of the unit cell, while the intensity distribution in C_{60} is fairly even within the first two BZs.

C_{60} growth on different substrates

C_{60} has been successfully grown on a number of substrates. In comparison with atomic crystals, for which films typically relax if exposed to values of epitaxial strain larger than 2-3%, molecular crystals are more malleable and can be expanded or compressed by more than 5%. Table S1 shows a list of the reconstructions reported so far on different substrates. In three cases the band structure was mapped by ARPES, with differing results: on Ag(111) the low energy states are hole-like [29], on Ag(100) they are electron-like [30], and same on Cu(111)

but with a very different dispersion [31]. In this last case, as noted in the main text, we believe that the observed bands are due to an interface state.

Naively one would expect lattice compression to favor metallicity via an increase of the bandwidth W , yet no obvious trend can be pointed out based on these sparse results since the effect on U of the different reconstructions cannot be easily estimated. Note also that, out of the list in Table S1, only Refs. [29], [64] and [65] are on monolayer-thick films. Whereas Ref. [29] finds a more standard $(2\sqrt{3} \times 2\sqrt{3})R30^\circ$ superstructure on Ag(111), confirmed later also in Ref. [66], Ref. [64] reports on Pb(111) a large unit cell with a moiré wavelength λ of 34Å aligned with the C_{60} lattice, and another of 46Å with a twist angle of 11°, and Ref. [65] finds $\lambda \simeq 70\text{Å}$ on Au(111) and a rotational mismatch of 14.5°. Based on the numerous reconstructions reported for thicker films it appears that the potential of fullerides for fabricating moiré heterostructures remains largely unexploited.

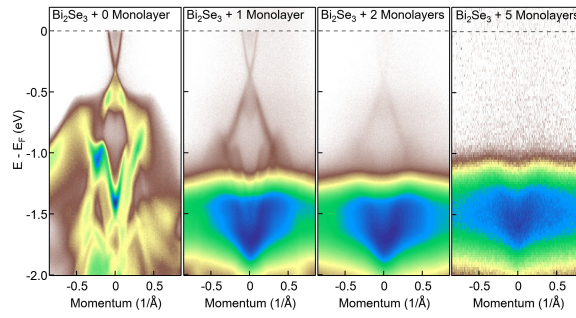


FIG. S5. From left to right, electronic structure measured along the ΓM high-symmetry direction for increasing C_{60} coverage from 0 to 3 monolayers on a $Bi_2Se_3(0001)$ substrate.

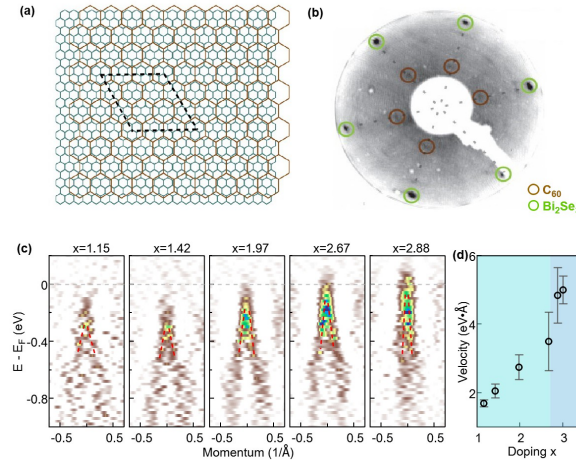


FIG. S6. **Band structure evolution in proximity of half filling.** **a** Real space sketch of the C_{60} balls on the $Bi_2Se_3(0001)$ substrate (the additional atom (C_{60} molecule) at the center of each small (large) hexagon is omitted for clarity). The rhomboids indicate the possible moiré pattern defined by the relative position of the C_{60} ball and the Se atom. **b** LEED pattern measured at 34 eV for a single monolayer of C_{60} . **c** Second derivative data taken along the momentum direction for the indicated doping levels. The dashed lines are guides to the eye. **d** The band velocity extracted as $E = v \cdot k_{\parallel}$ assuming a linear dispersion for consistency across the doping range in panel **c**. The data point at $x = 3$ is taken from Fig. 4(d).

* alanzara@lbl.gov

- [1] M. Kiguchi, K.-i. Iizumi, K. Saiki, and A. Koma, *Applied surface science* **212**, 101 (2003).
- [2] L.-L. Wang and H.-P. Cheng, *Physical Review B* **69**, 045404 (2004).
- [3] K. Kim, T. H. Lee, E. J. G. Santos, P. S. Jo, A. Salleo, Y. Nishi, and Z. Bao, *ACS Nano* **9**, 5922 (2015), pMID: 26027690.
- [4] C. Ojeda-Aristizabal, E. J. G. Santos, S. Onishi, A. Yan, H. I. Rasool, S. Kahn, Y. Lv, D. W. Latzke, J. Velasco, M. F. Crommie, M. Sorensen, K. Gotlieb, C.-Y. Lin, K. Watanabe, T. Taniguchi, A. Lanzara, and A. Zettl, *ACS Nano* **11**, 4686 (2017), pMID: 28437062, <https://doi.org/10.1021/acsnano.7b00551>.
- [5] N. Haag, D. Lüftner, F. Haag, J. Seidel, L. L. Kelly, G. Zamborlini, M. Jugovac, V. Feyer, M. Aeschlimann, P. Puschnig, M. Cinchetti, and B. Stadtmüller, *Physical Review B* **101**, 165422 (2020).
- [6] Y. Cao, V. Fatemi, A. Demir, S. Fang, S. L. Tomarken, J. Y. Luo, J. D. Sanchez-Yamagishi, K. Watanabe, T. Taniguchi, and E. Kaxiras, *Nature* **556**, 80 (2018).
- [7] Y. Cao, V. Fatemi, S. Fang, K. Watanabe, T. Taniguchi, E. Kaxiras, and P. Jarillo-Herrero, *Nature* **556**, 43 (2018).
- [8] M. M. Ugeda, A. J. Bradley, S.-F. Shi, H. Felipe, Y. Zhang, D. Y. Qiu, W. Ruan, S.-K. Mo, Z. Hussain, Z.-X. Shen, *et al.*, *Nature materials* **13**, 1091 (2014).
- [9] L. Wang, E.-M. Shih, A. Ghiotto, L. Xian, D. A. Rhodes, C. Tan, M. Claassen, D. M. Kennes, Y. Bai, B. Kim, K. Watanabe, T. Taniguchi, X. Zhu, J. Hone, A. Rubio, A. N. Pasupathy, and C. R. Dean, *Nature Materials* **19**, 861 (2020).
- [10] Y. Xu, C. Horn, J. Zhu, Y. Tang, L. Ma, L. Li, S. Liu, K. Watanabe, T. Taniguchi, J. C. Hone, J. Shan, and K. F. Mak, *Nature Materials* **20**, 645 (2021).

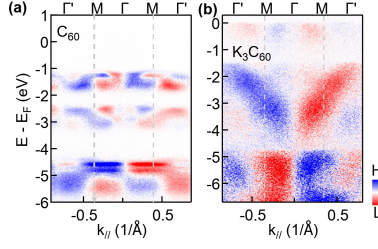


FIG. S7. (a) Difference between band dispersion of undoped C₆₀ measured with left and right circularly polarized light for C₆₀. (b) Same as (a) for K₃ C₆₀. Note that the energy scale in (b) is shifted down for 0.7 eV relatively to that in (a) to align the HOMO/HOMO1 states.

substrate	Ag(111)	Al(111)	Pt(111)	Pb(111)	Au(111)
structure	$2\sqrt{3} \times 2\sqrt{3}R30^\circ$	$2\sqrt{3} \times 2\sqrt{3}R30^\circ$	$\sqrt{13} \times \sqrt{13}R13.9^\circ$	HOC	$2\sqrt{3} \times 2\sqrt{3}R30^\circ$
intermolecular distance (Å)	10.01	9.91	10.005	10.0	9.99
expansion(+)/compression(-)	1.1%	-0.1%	1.1%	1.0%	-0.9%
reference	[29]	[67]	[68]	[64]	[69]

substrate	Cu(111)	Graphite	Si(111)	Si(100)	GaAs(001)	Au(111)
structure	$\sqrt{7} \times \sqrt{7}$ and 2×2 disordered and linear-wall maze	Unknown	7×7	2×1	2×6	$\sqrt{589} \times \sqrt{589}R14.5$
intermolecular distance (Å)	9.654 ~ 10.224	10.5	unknown	10.4	10.20	10.02
expansion(+)/compression(-)	-2.5 ~ 3.3%	6.1%	unknown	5.1%	3.0%	1.2%
reference	[70]	[71]	[72]	[73]	[74]	[65]

substrate	Pt(111)	Cd(0001)	Cu(111)	Ag(100)	Bi ₂ Se ₃ (0001)
structure	$2\sqrt{3} \times 2\sqrt{3}R30^\circ$	Unknown	4×4	$c(6 \times 4)$	7×7
intermolecular distance (Å)	9.5	10.5	10.2	10.42/11.56 (not hex)	9.66
expansion(+)/compression(-)	-4.0%	6.1%	3.0%	4.2/5.6%	-3.4%
reference	[75]	[76]	[77]	[30]	This work

TABLE S1. Reconstructions and periodicities reported for C₆₀ on several substrates. HOC = high order commensurate (multiple sizes and orientations).

- [11] Materials and methods are available as supplementary materials.
- [12] D. W. Latzke, C. Ojeda-Aristizabal, J. D. Denlinger, R. Reno, A. Zettl, and A. Lanzara, ACS Nano **13**, 12710 (2019).
- [13] O. Gunnarsson, Reviews of modern physics **69**, 575 (1997).
- [14] M. Capone, M. Fabrizio, C. Castellani, and E. Tosatti, Reviews of Modern Physics **81**, 943 (2009).
- [15] Y. Takabayashi and K. Prassides, Philosophical Transactions of the Royal Society A: Mathematical, Physical and Engineering Sciences **374**, 20150320 (2016).
- [16] M. Capone, M. Fabrizio, C. Castellani, and E. Tosatti, Science **296**, 2364 (2002).
- [17] P. Durand, G. R. Darling, Y. Dubitsky, A. Zaopo, and M. J. Rosseinsky, Nature Materials **2**, 605 (2003).
- [18] N. Manini and E. Tosatti, arXiv preprint cond-mat/0602134 (2006).
- [19] F. Steglich and S. Wirth, Reports on Progress in Physics **79**, 084502 (2016).
- [20] H. M. Yamamoto, Bulletin of the Chemical Society of Japan **94**, 2505 (2021).
- [21] C. Chen, L. Tjeng, P. Rudolf, G. Meigs, J. Rowe, J. Chen, J. McCauley, A. Smith, A. McGhie, and W. Romanow, Nature **352**, 603 (1991).
- [22] M. Merkel, M. Knupfer, M. Golden, J. Fink, R. Seemann, and R. Johnson, Physical Review B **47**, 11470 (1993).
- [23] G. Wertheim and D. Buchanan, Physical Review B **47**, 12912 (1993).
- [24] J. L. McChesney, A. Bostwick, T. Ohta, T. Seyller, K. Horn, J. González, and E. Rotenberg, Physical Review Letters **104**, 136803 (2010).
- [25] C. Hwang, D. A. Siegel, S.-K. Mo, W. Regan, A. Ismach, Y. Zhang, A. Zettl, and A. Lanzara, Scientific Reports **2** (2012), 10.1038/srep00590.
- [26] S. Kawasaki, J. Fukui, T. Motoyama, Y. Suzuki, S. Shibusaki, and G. qing Zheng, Journal of the Physical Society of Japan **82**, 014709 (2013).

- [27] V. Brouet, W. Yang, X. Zhou, Z. Hussain, and Z. Shen, *Journal of Physics and Chemistry of Solids* **67**, 218 (2006).
- [28] R. Hesper, L. Tjeng, A. Heeres, and G. Sawatzky, *Physical Review B* **62**, 16046 (2000).
- [29] W. Yang, V. Brouet, X. Zhou, H. J. Choi, S. G. Louie, M. L. Cohen, S. Kellar, P. Bogdanov, A. Lanzara, and A. Goldoni, *Science* **300**, 303 (2003).
- [30] V. Brouet, W. Yang, X. Zhou, H. Choi, S. Louie, M. Cohen, A. Goldoni, F. Parmigiani, Z. Hussain, and Z. Shen, *Physical review letters* **93**, 197601 (2004).
- [31] W. W. Pai, H. Jeng, C.-M. Cheng, C.-H. Lin, X. Xiao, A. Zhao, X. Zhang, G. Xu, X. Shi, and M. Van Hove, *Physical Review Letters* **104**, 036103 (2010).
- [32] D. W. Latzke, C. Ojeda-Aristizabal, S. M. Griffin, J. D. Denlinger, J. B. Neaton, A. Zettl, and A. Lanzara, *Physical Review B* **99**, 045425 (2019).
- [33] P. W. Stephens, L. Mihaly, P. L. Lee, R. L. Whetten, S.-M. Huang, R. Kaner, F. Deiderich, and K. Holczer, *Nature* **351**, 632 (1991).
- [34] J. L. Martins and N. Troullier, *Physical Review B* **46**, 1766 (1992).
- [35] Q. Zhu, D. E. Cox, and J. E. Fischer, *Physical Review B* **51**, 3966 (1995).
- [36] G. Oszlányi, G. Bortel, G. Faigel, M. Tegze, L. Gránásy, S. Pekker, P. W. Stephens, G. Bendele, R. Dinnebier, G. Mihály, A. Jánossy, O. Chauvet, and L. Forró, *Physical Review B* **51**, 12228 (1995).
- [37] T. Pichler, M. Knupfer, M. S. Golden, S. Haffner, R. Friedlein, J. Fink, W. Andreoni, A. Curioni, M. Keshavarz-K, C. Bellavia-Lund, A. Sastre, J.-C. Hummelen, and F. Wudl, *Physical Review Letters* **78**, 4249 (1997).
- [38] R. Macovez, P. Rudolf, I. Marenne, L. Kjeldgaard, P. A. Brühwiler, T. Pichler, P. Vilmercati, R. Larciprete, L. Petaccia, G. Bertoni, and A. Goldoni, *Physical Review B* **75**, 195424 (2007).
- [39] D. Konarev, S. Khasanov, A. Otsuka, M. Maesato, G. Saito, and R. Lyubovskaya, *Angewandte Chemie International Edition* **49**, 4829 (2010).
- [40] S. C. Erwin and W. E. Pickett, *Science* **254**, 842 (1991).
- [41] O. Gunnarsson, E. Koch, and R. M. Martin, *Physical Review B* **54**, R11026 (1996).
- [42] J. E. Han, E. Koch, and O. Gunnarsson, *Phys. Rev. Lett.* **84**, 1276 (2000).
- [43] S. Satpathy, V. P. Antropov, O. K. Andersen, O. Jepsen, O. Gunnarsson, and A. I. Liechtenstein, *Physical Review B* **46**, 1773 (1992).
- [44] Y. Wang, Y. He, K. Wohlfeld, M. Hashimoto, E. W. Huang, D. Lu, S.-K. Mo, S. Komiyama, C. Jia, B. Moritz, Z.-X. Shen, and T. P. Devereaux, *Communications Physics* **3** (2020), 10.1038/s42005-020-00480-5.
- [45] A. H. Castro Neto, F. Guinea, N. M. R. Peres, K. S. Novoselov, and A. K. Geim, *Rev. Mod. Phys.* **81**, 109 (2009).
- [46] Y. Xia, D. Qian, D. Hsieh, L. Wray, A. Pal, H. Lin, A. Bansil, D. Grauer, Y. S. Hor, R. J. Cava, *et al.*, *Nature physics* **5**, 398 (2009).
- [47] M. König, S. Wiedmann, C. Brüne, A. Roth, H. Buhmann, L. W. Molenkamp, X.-L. Qi, and S.-C. Zhang, *Science* **318**, 766 (2007).
- [48] P. Zhang, K. Yaji, T. Hashimoto, Y. Ota, T. Kondo, K. Okazaki, Z. Wang, J. Wen, G. D. Gu, H. Ding, and S. Shin, *Science* **360**, 182 (2018).
- [49] S. Borisenko, Q. Gibson, D. Evtushinsky, V. Zabolotnyy, B. Büchner, and R. J. Cava, *Physical review letters* **113**, 027603 (2014).
- [50] M. Neupane, S.-Y. Xu, R. Sankar, N. Alidoust, G. Bian, C. Liu, I. Belopolski, T.-R. Chang, H.-T. Jeng, H. Lin, *et al.*, *Nature communications* **5**, 1 (2014).
- [51] Z. K. Liu, B. Zhou, Y. Zhang, Z. J. Wang, H. M. Weng, D. Prabhakaran, S.-K. Mo, Z. X. Shen, Z. Fang, X. Dai, Z. Hussain, and Y. L. Chen, *Science* **343**, 864 (2014).
- [52] M.-Q. Ren, S. Han, S.-Z. Wang, J.-Q. Fan, C.-L. Song, X.-C. Ma, and Q.-K. Xue, *Physical Review Letters* **124** (2020), 10.1103/physrevlett.124.187001.
- [53] S. Zhou, G.-H. Gweon, J. Graf, A. Fedorov, C. Spataru, R. Diehl, Y. Kopelevich, D.-H. Lee, S. G. Louie, and A. Lanzara, *Nature physics* **2**, 595 (2006).
- [54] Due to the completely different fermiology, it is our best guess that the band structure reported for doped C₆₀ on Cu(111) in Ref. 29 be due to an interface state and largely unrelated to the K₃C₆₀ physics discussed here.
- [55] R. W. Lof, M. A. van Veenendaal, B. Koopmans, H. T. Jonkman, and G. A. Sawatzky, *Physical Review Letters* **68**, 3924 (1992).
- [56] L. Hou, X. Cui, B. Guan, S. Wang, R. Li, Y. Liu, D. Zhu, and J. Zheng, *Nature* **606**, 507 (2022).
- [57] E. Meirzadeh, A. M. Evans, M. Rezaee, M. Milich, C. J. Dionne, T. P. Darlington, S. T. Bao, A. K. Bartholomew, T. Handa, D. J. Rizzo, R. A. Wiscons, M. Reza, A. Zangabadi, N. Fardian-Melamed, A. C. Crowther, P. J. Schuck, D. N. Basov, X. Zhu, A. Giri, P. E. Hopkins, P. Kim, M. L. Steigerwald, J. Yang, C. Nuckolls, and X. Roy, *Nature* **613**, 71 (2023).
- [58] S. Hasegawa, T. Miyamae, K. Yakushi, H. Inokuchi, K. Seki, and N. Ueno, *Physical Review B* **58**, 4927 (1998).
- [59] A. Kumar, A. Podhorodecki, J. Misiewicz, D. K. Avasthi, and J. C. Pivin, *Journal of Applied Physics* **105**, 024314 (2009).
- [60] S. Hasegawa, T. Miyamae, K. Yakushi, H. Inokuchi, K. Seki, and N. Ueno, *Phys. Rev. B* **58**, 4927 (1998).
- [61] A. Rüdel, R. Hentges, U. Becker, H. S. Chakraborty, M. E. Madjet, and J. M. Rost, *Phys. Rev. Lett.* **89**, 125503 (2002).
- [62] X.-X. Wang, Y.-B. Xu, H.-N. Li, W.-H. Zhang, and F.-Q. Xu, *Journal of Electron Spectroscopy and Related Phenomena* **165**, 20 (2008).
- [63] D. Toffoli, M. Stener, G. Fronzoni, and P. Decleva, *Chemical Physics Letters* **516**, 154 (2011).
- [64] H. I. Li, K. J. Franke, J. I. Pascual, L. W. Bruch, and R. D. Diehl, *Phys. Rev. B* **80**, 085415 (2009).
- [65] G. Schull and R. Berndt, *Phys. Rev. Lett.* **99**, 226105 (2007).
- [66] H. I. Li, K. Pussi, K. J. Hanna, L.-L. Wang, D. D. Johnson, H.-P. Cheng, H. Shin, S. Curtarolo, W. Moritz, J. A. Smerdon, R. McGrath, and R. D. Diehl, *Phys. Rev. Lett.* **103**, 056101 (2009).
- [67] M. Stengel, A. D. Vita, and A. Baldereschi, *Phys. Rev. Lett.* **91**, 166101 (2003).
- [68] R. Felici, M. Pedio, F. Borgatti, S. Iannotta, M. Capozzi, G. Ciullo, and A. Stierle, *Nature materials* **4**, 688 (2005).
- [69] E. I. Altman and R. J. Colton, *Phys. Rev. B* **48**, 18244 (1993).
- [70] W. W. Pai, C.-L. Hsu, M. C. Lin, K. C. Lin, and T. B. Tang, *Phys. Rev. B* **69**, 125405 (2004).
- [71] Z. Li, *Surface Science* **441**, 366 (1999).

- [72] L. Aversa, S. Taioli, M. V. Nardi, R. Tatti, R. Verucchi, and S. Iannotta, *Frontiers in Materials* **2**, 46 (2015).
- [73] T. Hashizume, X.-D. Wang, Y. Nishina, H. Shinohara, Y. Saito, Y. Kuk, and T. Sakurai, *Japanese Journal of Applied Physics* **31**, L880 (1992).
- [74] Q. Xue, T. Ogino, Y. Hasegawa, H. Shinohara, and T. Sakurai, *Phys. Rev. B* **53**, 1985 (1996).
- [75] X. Q. Shi, A. B. Pang, K. L. Man, R. Q. Zhang, C. Minot, M. S. Altman, and M. A. Van Hove, *Phys. Rev. B* **84**, 235406 (2011).
- [76] Z. Wang, M. Tao, D. Yang, Z. Li, M. Shi, K. Sun, J. Yang, and J. Wang, *International Journal of Molecular Sciences* **22**, 6880 (2021).
- [77] T. Hashizume and T. Sakurai, *Surface Review and Letters* **03**, 905 (1996).